Research Article Vol. 26, No. 17 | 20 Aug 2018 | OPTICS EXPRESS 22075

Optics EXPRESS

Optomechanical antennas for on-chip beam-steering

CHRISTOPHER J. SARABALIS,[1,2,*] **RAPHAËL VAN LAER,**[1,2] **AND AMIR H. SAFAVI-NAEINI**[1]

[1] *Department of Applied Physics, and Ginzton Laboratory, Stanford University, Stanford, California 94305, USA*
[2] *These authors contributed equally to this work*
[*] *sicamor@stanford.edu*

Abstract: Rapid and low-power control over the direction of a radiating light field is a major challenge in photonics and a key enabling technology for emerging sensors and free-space communication links. Current approaches based on bulky motorized components are limited by their high cost and power consumption, while on-chip optical phased arrays face challenges in scaling and programmability. Here, we propose a solid-state approach to beam-steering using optomechanical antennas. We combine recent progress in simultaneous control of optical and mechanical waves with remarkable advances in on-chip optical phased arrays to enable low-power and full two-dimensional beam-steering of monochromatic light. We present a design of a silicon photonic system made of photonic-phononic waveguides that achieves 44° field of view with 880 resolvable spots by sweeping the mechanical wavelength with about a milliwatt of mechanical power. Using mechanical waves as nonreciprocal, active gratings allows us to quickly reconfigure the beam direction, beam shape, and the number of beams. It also enables us to distinguish between light that we send and receive.

1. Introduction

Fiber-coupled photonic circuits are powerful tools in our information infrastructure. In order to leverage these circuits to control and analyze light in our environment, we need to control how they radiate and absorb radiation. Gratings are an established way of controlling how photonic circuits radiate. They are dispersive: tuning the wavelength of light incident on a grating changes the angle at which it is scattered. With a tunable laser gratings can thus steer light in one dimension [1, 2]. When incorporated with phase-shifters into an array, they can steer in two dimensions [3–8]. The size, weight, power, and cost of these integrated beam-steering systems is lower than the motorized optical gimbals currently used with free-space optical systems for lidar, optical wireless communication [9, 10], and free-space optical interconnects [11]. The growing presence of autonomous systems, such as self-driving cars, motivates the development of mass-manufacturable photonic systems. With low-power on-chip beam-steering, a host of remote sensing, communication, and display applications comes into reach.

With angular dispersion as the steering mechanism the etched grating's period Λ fixes a relation between optical wavelength λ and scattering angle θ. In contrast, with the ability to tune the grating period Λ, a monochromatic beam can be formed and directed. Sound is a naturally tunable optical grating. An acoustic wave containing multiple wavelengths scatters light into multiple angles as realized in pioneering work on acousto-optic beam deflectors [12–14]. A progression to guided-wave, collinear systems [15, 16] and arrays [17] in Ti-diffused and proton-exchanged lithium niobate waveguides enabled large fields of view for monochromatic light. These low index-contrast lithium niobate waveguides limit integrability, resolution, and efficiency. We address these limitations by embracing high index-contrast, subwavelength-scale silicon waveguides to be incorporated into a dense phased array. These waveguides – engineered

#328356 https://doi.org/10.1364/OE.26.022075
Journal © 2018 Received 13 Apr 2018; revised 14 Jul 2018; accepted 16 Jul 2018; published 10 Aug 2018

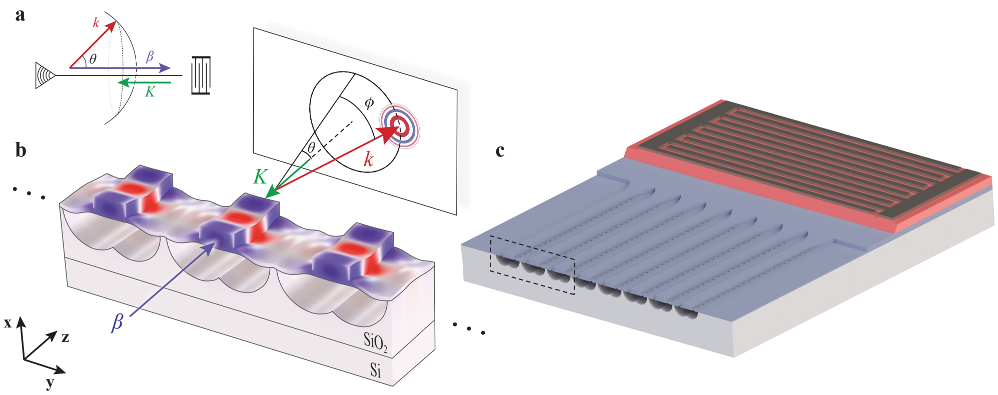

Fig. 1. (a) A mechanical wave with wavevector K scatters a guided optical wave (β) into free-space (k) at an angle θ. A single antenna scatters light into a cone. Sweeping the mechanical frequency, and therefore K, steers the cone through a range of angles θ. (b) Incorporating these antennas into a phased array forms a beam in the far-field directed into angle ϕ. Antennas consist of partially released silicon ridge waveguides each of which supports guided optical and guided mechanical modes. The displacement field $\mathbf{u}$ that scatters guided light (color representing the electric displacement field D_x) out at $\theta = 60°$. (c) Light from a phase-shifter/splitter network (not shown) counterpropagates with mechanical waves driven by a piezoelectric transducer. An interdigital transducer (gray) is patterned on a piezoelectric film (red) deposited on SOI (blue on white). The transducer injects mechanical waves with nanometer-scale displacement and milliwatt-level power into the silicon waveguides.

to guide both light and sound – have recently been shown to exhibit strong acousto-optic interactions between propagating waves with tailorable dispersion [18–20].

Here we develop the concept of an *optomechanical antenna* (OMA) and present a perturbative description of the coupling between guided and radiated light by sound analogous to cavity optomechanics and Brillouin scattering [18–23]. After illustrating the scattering process for a slab waveguide, we explore the optical and mechanical co-design of an OMA compatible with silicon photonics and practical for a phased array antenna. We will show that such an OMA can scatter light in millimeters with only hundreds of microwatts of mechanical power. We conclude with an outline of this device's performance, an account of the effects of disorder, and an outlook on the new capabilities of this approach.

2. Mechanics as a dynamic grating

In an optomechanical antenna [Fig. 1(a)] a guided optical wave with electric field $\mathbf{E}\ \exp(i\beta z - i\omega t)$ is scattered by a guided mechanical wave with displacement field $\mathbf{u}\ \exp(-iKz - i\Omega t)$ into radiating light with electric field $\mathbf{E}_\mathrm{r}\ \exp(i\mathbf{k}\cdot\mathbf{r} - i\omega_\mathrm{r} t)$. Energy and momentum conservation for the counter-propagating, anti-Stokes process

$$\omega_\mathrm{r} = \omega + \Omega \tag{1}$$

$$k\ \cos\theta = \beta - K, \tag{2}$$

determine the scattering angle θ [Fig. 1(a)]. The equations above describe the copropagating, Stokes process by reversing the sign of Ω. Under these phase-matching constraints, a single antenna radiates into a cone and a phased array into a pair of beams above and below the array. A frequency-swept mechanical drive sweeps the beam angle θ across the field of view in microseconds – the time it takes a mechanical wave to traverse the antenna.

Analogous to the treatment of interactions in cavity optomechanics and Brillouin scattering, we perturbatively compute radiation from an OMA. Mechanical deformations vary the dielectric permittivity $\varepsilon \longrightarrow \varepsilon + \delta_u \varepsilon \cdot \mathbf{u}$ with photoelastic and moving-boundary contributions to the scattering given explicitly in appendix C. Making a first Born approximation (see appendix C) [24], we have

$$\left(\nabla \times \nabla \times - \mu \varepsilon \omega^2\right) \mathbf{E}_\mathrm{r} = i \omega \mu \mathbf{J}_\mathrm{om} \tag{3}$$

where the optomechanically-induced polarization current

$$\mathbf{J}_\mathrm{om} = -i\omega \left(\delta_u \varepsilon \cdot \mathbf{u}\right) \mathbf{E} \tag{4}$$

is defined in terms of the unperturbed guided optical and mechanical modes $\mathbf{E}$ and $\mathbf{u}$. The result is a set of inhomogeneous equations which we solve for the radiated electric field $\mathbf{E}_\mathrm{r}$.

Coupling to radiation causes decay of the optical power $\mathcal{P}(z)$ in the waveguide. From perturbation theory we find that the matrix element coupling $\mathbf{E}$ and $\mathbf{E}_\mathrm{r}$ scales as $u = \max|\mathbf{u}|$. By Fermi's Golden Rule, the radiated optical power per unit length is $\alpha = \alpha_\mathrm{m} u^2$ and therefore proportional to power in the mechanical wave $\mathcal{P}_\mathrm{m}$. Neglecting mechanical decay,

$$\mathcal{P}(z) = \mathcal{P}_0 e^{-\alpha_\mathrm{m} u^2 z}. \tag{5}$$

The scattering rate α_m is the rate of conversion between guided and radiating optical fields per unit length per the square of the mechanical deformation amplitude. In contrast to static gratings where the scattering rate is fixed by fabrication, modulating the mechanical power modulates the effective aperture $L_\mathrm{eff} = \alpha_\mathrm{m}^{-1} u^{-2}$ of an OMA.

3. Radiation of a slab waveguide

We begin by analyzing a simple OMA: a 220 nm thick silicon slab waveguide suspended in air. A typical scattering process is plotted in Fig. 2(a) where an antisymmetric mechanical Lamb wave scatters a counter-propagating guided transverse-electric (TE) optical mode into free space at $\theta = 45°$.

The slab waveguide is simple enough to admit to an analytical approach. A full coupled-mode description for roughness-induced scattering has been developed and is applicable to optomechanical scattering [25, 26]. We take a numerical approach easily extended to arbitrary geometries in which finite-element-method solutions of the uncoupled equations drive the inhomogeneous Eq. (3).

The scattering rates plotted in Fig. 2(b) show that nanometer-scale oscillations yield millimeter-scale effective apertures. Light which propagates with an effective index $n_\mathrm{eff} = 2.8$ scatters out symmetrically above and below the waveguide in the phase-matched region when $K/2\pi$ is between 1.2 $\mu\mathrm{m}^{-1}$ ($\theta = 0°$) and 2.5 $\mu\mathrm{m}^{-1}$ ($\theta = 180°$). The moving-boundary term dominates the optomechanical interaction while the photoelastic contribution is 50× smaller for this OMA (see appendix B.3). The interaction between TE guided light and Lamb waves is captured by an optomechanically-induced polarization current along $\hat{y}$

$$\mathbf{J}_\mathrm{om} = -i\omega \Delta\varepsilon E_y u_x \hat{y}, \tag{6}$$

which drives $\hat{y}$-polarized TE optical fields in the surrounding medium. For antisymmetric Lamb waves, the polarization currents induced on the top and bottom surfaces of the waveguide are 180° out-of-phase, but since $n t_\mathrm{Si} \approx \frac{\lambda}{2}$, they interfere constructively giving rise to strong scattering rates α. For the same reason, surface currents of symmetric Lamb waves interfere destructively such that the moving-boundary contribution to α is small detailed in appendix B.2.

Since the mechanical frequencies are much smaller than the optical frequency, they can be treated quasi-statically. Rather than the perturbative approach, the waveguide can be statically

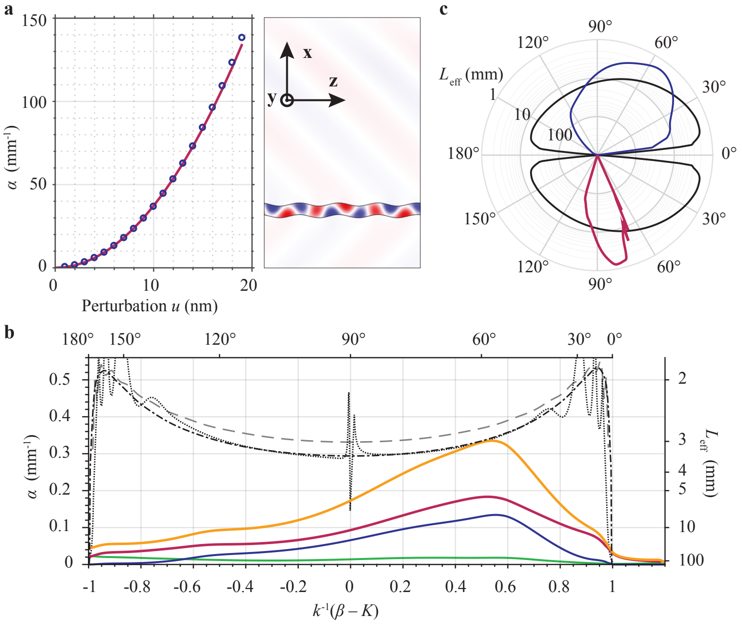

Fig. 2. (a) Scattering from the TE-polarized optical mode of a 220 nm thick suspended silicon slab is computed nonperturbatively and the electric displacement field D_y is plotted where the maximal displacement u is set to 30 nm for visibility of the radiated field. The single-sided scattering rate α is quadratic in u even for large displacements. (b) The displacement-normalized scattering rates for the slab and ridge OMA are plotted together for $u = 1$ nm. Slab rates plotted in black and gray are computed nonperturbatively in 2D (dotted) as well as perturbatively in 2D (dot-dash) and 3D (dashed). For the ridge OMA of section 4, radiation into the optical slab modes (green), air (blue), and the silicon handle (red) add to give the total scattering rate (yellow). (c) Normalizing the scattering rate by power, here 1 mW per antenna for a ridge OMA array and 1 mW per 1.41 μm for the slab, gives a practical measure of the field of view $\Delta\theta$. Tight confinement of the optical and mechanical energy in the transverse direction for the ridge OMA leads to enhanced radiation for a range of angles compared to the slab case.

deformed by $\mathbf{u}$ and solved for the radiating field by frequency or time-domain methods. The quasi-static, nonperturbative approach agrees well with perturbative calculations and results from literature (see appendix A).

While easily compared to scattering rates for etched gratings, the displacement-normalized α_m hides an important aspect of optomechanical antenna performance: the mechanical power. The fixed-power antenna functions [Fig. 2(c)] fall rapidly at higher angles θ since K and therefore $\mathcal{P}_\mathrm{m} \propto \Omega^2$ increase. In comparison to OMAs employing surface acoustic waves in lithium niobate [17], suspended structures are compliant and tightly confine the mechanical energy of their modes. This reduces the mechanical power $\mathcal{P}_\mathrm{m}$ needed to achieve a given scattering rate α_m by orders of magnitude.

4. Optomechanical antennas for silicon photonics

Having explored a two-dimensional optomechanical antenna, we add transverse structure to our calculations to yield a design for an OMA practical for an array and compatible with microelectronics manufacturing. In doing so, the mechanical waves of the slab are replaced by a multi-moded mechanical response of the core and socket of the waveguide in Fig. 1(b). Mixing

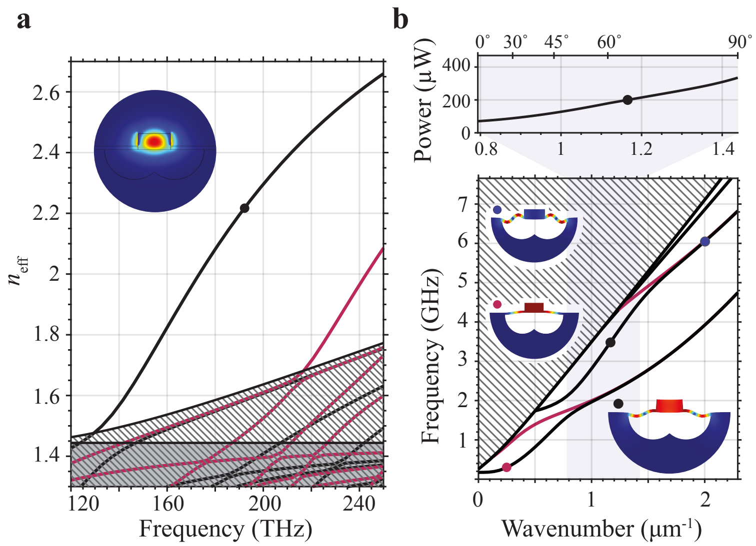

Fig. 3. The ridge OMA guides light and sound supporting a range of mechanical modes over which the 193 THz optical mode (dot on black band of (a) E_y inset) can be scattered from 0° to 90° (shaded in blue). The mechanical power needed to achieve max $|u_z| = 1$ nm oscillations of the core is plotted above the bands of (b) Inset plots of the displacement show the low K behavior (red) where the mode resembles the fundamental Lamb mode of a uniform, clamped membrane. The first excited symmetric mode in the shaded region (black dot) is the mode of interest with scattering rates plotted in Fig. 2. After the anticrossing the mode is expelled from the core into the sockets (blue dot). In (a), the antisymmetric (with respect to y-reflection) and symmetric bands are plotted in black and red, respectively. In (b), symmetric and antisymmetric bands are plotted in black and red, respectively. In both band diagrams, the continuum of radiation modes of the 50 nm SOI stack are hatched.

between core and socket modes becomes an important feature of the antenna's optomechanical response.

The OMA we describe is designed for 220 nm silicon-on-insulator (SOI) common in silicon photonics. A ridge waveguide is defined by a 170 nm partial etch, leaving a compliant 50 nm socket connecting the 450 nm wide optical core to the substrate. The ridge is partially released leaving a 1.33 μm wide suspended region. This width allows for subwavelength 1.41 μm pitched arrays with a transverse field of view $\Delta\phi$ of up to 67°.

This OMA supports both guided optical and guided mechanical modes. At 193 THz optical waves are confined to the waveguide core and have an effective index $n_{\mathrm{eff}} = 2.33$, well above the slab modes of the 50 nm SOI stack (hatched in Fig. 3(a)). The effective index sets the range of wavevectors $K \in 2\pi \times [0.86, 2.15]\ \mu\mathrm{m}^{-1}$ that phase-match β to free-space k. For these wavevectors, Lamb-like flexural modes of the waveguide have lower phase velocities than any other mechanical excitation in the system. They comprise bands that fall below the cone of surface and bulk waves of the 50 nm SOI stack, represented by the hatched region in Fig. 3. Consequently, they do not suffer mechanical radiation losses in the absence of disorder [20, 27].

Mechanical modes of the structure can be understood in terms of waves in the sockets and waves in the core. Only motion of the core causes the antenna to radiate, directing our attention to the first excited symmetric band of Fig. 3(b). The fast band of the core mixes with the slow bands of the socket giving rise to avoided crossings at $K/2\pi$ of 0.8 μm^{-1} and 1.5 μm^{-1}. Below and above the avoided crossings, the sockets are mechanically decoupled by the core. This leads to nearly degenerate symmetric (black) and antisymmetric (red) bands. The motion of the core is

Table 1. **Optomechanical antenna properties.**

Antenna property	
Antenna length L_{eff}	2 mm
Mechanical power $\mathcal{P}_{\text{m}}$	2 mW
Transducer bandwidth $\frac{\Delta\Omega}{2\pi}$	1.6 GHz
Field of view $\Delta\theta$	44°
Spot size $\delta\theta$	0.05°
Resolvable spots N_θ	880
Optical bandwidth $\frac{\Delta\omega}{2\pi}$	39 GHz
Mechanical bandwidth $\frac{\Delta\Omega_{\text{m}}}{2\pi}$	2 MHz

suppressed in these degenerate bands, and therefore there is no optomechanical coupling.

The scattering rates are computed perturbatively and plotted in Fig. 2(b) alongside the results for a slab. The scattering rate α is peaked at $\theta \approx 60°$ and falls off near the avoided crossings. Since the scattering rates are normalized by the maximum displacement of the core and not by power, these tails come from changes to the mechanical mode profile. Radiation into air is slightly weaker than into silicon. The latter is small but nonzero even when radiation into air is disallowed by phase-matching $\left|k^{-1}(\beta - K)\right| > 1$. The ridge OMA scatters out at nearly half the rate of the slab.

Despite the effects of mechanical mode mixing, the ridge OMA retains a large field of view as shown by the power-normalized antenna function of Fig. 2(c). For less than a milliwatt of mechanical power per antenna, corresponding to approximately 1 nm maximal displacement, scattering lengths of 2 mm can be achieved over $\Delta\theta = 13°$. Doubling either the power or the scattering length more than doubles the field of view $\Delta\theta = 44°$.

A microwave-driven, electromechanical transducer could excite the milliwatt-scale mechanical waves needed to efficiently scatter light out of the array. The coherent optical transduction schemes demonstrated in SOI would here exceed the power-handling thresholds for silicon waveguides. This follows from the discrepancy between optical and mechanical frequencies. A milliwatt mechanical wave corresponds to a phonon flux on the order of 10^{21} Hz. Achieving the same flux of optical photons requires 100 W whereas microwave photons can be converted to phonons with high efficiency by piezoelectric or capacitive electromechanical transducers. Our work motivates the integration of microwave-driven, electromechanical transducers into the silicon photonics platform [28].

5. Optics of optomechanical antennas

In the previous sections we designed an optomechanical antenna that can be integrated into a silicon photonic phased array. Here we discuss the main properties of its radiation pattern.

In the far-field the beam radiated from an OMA array is governed by Fraunhofer diffraction. For an ideal radiator where $\mathbf{J}_{\text{om}}$ does not vary in the longitudinal direction and remains coherent over a length L_{eff}, the far-field spot size is $\delta\theta = \lambda/(L_{\text{eff}} \sin\theta)$. The polar field of view $\Delta\cos\theta = \Delta K/k$

is set by the range of wavevectors ΔK for which α is large as quantified in Fig. 2(c). A full system requires an efficient mechanical transducer and coupling structure with bandwidth $\Delta\Omega$ over this range. Assuming negligible mechanical group velocity dispersion, the number of resolvable spots is the mechanical transit time-bandwidth product $N_\theta = \Delta\theta/\delta\theta = \tau_{\mathrm{m}}\Delta\Omega/2\pi$.

Since L_{eff} plays an important role in beam quality, we quantify sources of spatial decay and decoherence of $\mathbf{J}_{\mathrm{om}}$ that limit L_{eff}. Variations in the amplitude and phase of $\mathbf{J}_{\mathrm{om}}$ arise from optical and mechanical decay, as well as dephasing due to geometric disorder [29–32] and thermal fluctuations.

As light and sound propagate along the antennas, the phase of $\mathbf{J}_{\mathrm{om}}$ accumulates an error $\delta\varphi(z)$. This differs from beam-steering systems that use spatial light modulators [33], MEMS micromirrors [34, 35], or microlens arrays [36] where light interacts with the device only over a small distance. For fluctuations $\delta\beta(z)$ and $\delta K(z)$ spatially correlated over $\xi \ll L_{\mathrm{eff}}$, the phase error $\delta\varphi(z)$ diffuses along the antennas and is Gaussian-distributed with its variance growing linearly with z. We define L_φ as the length after which the phase variance $\langle\delta\varphi^2(z)\rangle$ averaged along the antennas equals π^2. This dephasing length L_φ depends on the relative propagation direction of the guided optical and mechanical waves. In the counter-propagating case we find

$$\left\langle \delta\varphi^2\left(z\right)\right\rangle = S_{\beta\beta}[0]z + S_{KK}[0](L-z) \tag{7}$$

where $S_{\beta\beta}$ and S_{KK} are the power spectral densities of $\delta\beta$ and δK (see appendix D for a derivation).

Geometric fluctuations δX_l, indexed by l, shift β by $\delta\beta(z) = \sum_l \partial_l\beta\delta X_l(z)$ such that for stationary noise with correlations

$$\langle\delta X_l\left(\Delta z\right)\delta X_l\left(0\right)\rangle = \sigma_l^2 e^{-|\Delta z|/\xi_l} \tag{8}$$

we get $S_{\beta\beta}[0] = 2\sum_l(\partial_l\beta\sigma_l)^2\xi_l$ and similarly for K. Slow drifts in X_l (large ξ_l) are more limiting than roughness since they lead to more rapid phase accumulation along each antenna. Therefore the dephasing length is

$$L_\varphi = \frac{2\pi^2}{S_{\beta\beta}[0] + S_{KK}[0]} \tag{9}$$

In the copropagating case we similarly obtain $\langle\delta\varphi^2(z)\rangle = S_{k_{||}k_{||}}[0]z$ with $\delta k_{||}(z) = \delta\beta(z) - \delta K(z)$, and the dephasing length $L_{\varphi,\mathrm{co}}$ is found by replacing the denominator and factor of 2 in the numerator of Eq. (9) by $S_{k_{||}k_{||}}[0]$.

We compute the geometric sensitivities to fluctuations $\partial_l\beta$ and $\partial_l K$ for different types of pertubations and find height variations to be the dominant source of dephasing. These results are collected in table 2 along with corresponding dephasing lengths. Our finite-element models predict similar optical and mechanical sensitivities to height disorder. The mechanical and optical sensitivities are usually of opposite sign: mechanical waves speed up when optical waves slow. We compute the mechanical sensitivities at a wavelength of $\Lambda = 842$ nm and frequency of $\Omega/2\pi = 3.42$ GHz such that the steering angle $\theta = 60°$ corresponds to the maximal scattering rate α [Fig. 2].

For the dephasing length estimates in table 2 the standard deviations σ_l are based on measurements of similar silicon photonic circuits [29–32] and correlation lengths ξ_l of 50 μm are assumed (see appendix D). In the purely optical case, the overall geometric dephasing length is $L_{\varphi,\beta} = 3.4$ mm. For counter-propagating optical and mechanical waves we have $L_\varphi = 1.7$ mm: about half of $L_{\varphi,\beta}$ as the optical and mechanical phase errors add incoherently. Further, the dephasing length for copropagating fields $L_{\varphi,\mathrm{co}} = 0.9$ mm is about four times smaller than $L_{\varphi,\beta}$ as the optical and mechanical phase errors subtract coherently.

Temperature gradients across the system also shift the phases of the guided optical and mechanical fields. Spatially inhomogeneous temperatures are analogous to geometric disorder.

Table 2. **Dephasing in a ridge OMA.**

Geometric dephasing	σ_l (nm)	$\partial_l\beta$ ($\mathrm{mm}^{-1}\mathrm{nm}^{-1}$)	$\partial_l K$ ($\mathrm{mm}^{-1}\mathrm{nm}^{-1}$)	$L_{\varphi,\beta}$ (mm)	L_φ (mm)	$L_{\varphi,\mathrm{co}}$ (mm)
Core width	0.5	7.8	-1.2	13	13	9.7
Core height	0.3	14.6	-12.2	10	6.1	3.1
Slab height	0.5	9.8	-11.9	8.1	3.3	1.7
Membrane width	2	−0.003	1.2	4021	35	34
Thermal dephasing	ΔT (K)	$\partial_T\beta$ ($\mathrm{mm}^{-1}\mathrm{K}^{-1}$)	$\partial_T K$ ($\mathrm{mm}^{-1}\mathrm{K}^{-1}$)	$L_{T,\beta}$ (mm)	L_T (mm)	$L_{T,\mathrm{co}}$ (mm)
	5	0.9	0.2	1.4	1.1	1.8

A temperature gradient ΔT across the antenna array results in thermal dephasing lengths of $L_{\mathrm{T}} = 2\pi/(|\partial_T(\beta + K)|\Delta T)$ in the counterpropagating and $L_{T,\mathrm{co}} = 2\pi/(|\partial_T k_{\parallel}|\Delta T)$ in the copropagating case (see appendix D). Careful thermal management can likely limit spatial temperature gradients to 5 K across the array [37] so we find $L_{\mathrm{T}} \approx 1.5$ mm in either case (table 2).

Optical and mechanical crosstalk between the waveguides in a phased array is another source of phase errors. Crosstalk splits the wavevectors of symmetric k_+ $(\cdots++++\ldots)$ and antisymmetric k_- $(\cdots+-+-\ldots)$ array supermodes, causing them to dephase after a length $L_{\mathrm{x}} = \pi/(k_+ - k_-)$. A 1.41 μm pitch array has an optical crosstalk length of $L_{\mathrm{x}} = 8.7$ mm.

Larger apertures yield narrower spots and higher resolution at the cost of the optical and mechanical modulation bandwidth. Although our control over mechanical wavevector K enables beam-steering at fixed optical frequency, optomechanical antennas are still dispersive. The optical bandwidth $\Delta\omega$ at fixed mechanical frequency is set by how much ω can be changed before a spot shifts by $\delta\theta$. We find $\Delta\omega/2\pi = 1/(\tau - \tau_{\mathrm{r}})$ with $\tau = L_{\mathrm{eff}}\, n_{\mathrm{g}}/c$ the transit time of the guided optical wave where n_{g} is the group index, and $\tau_{\mathrm{r}} = L_{\mathrm{eff}}\cos\theta/c$ the transit time of the radiating field across the aperture (see appendix F). Similarly, the mechanical transit time τ_{m} determines the mechanical bandwidth $\Delta\Omega_{\mathrm{m}}/2\pi = 1/\tau_{\mathrm{m}}$ within a spot at fixed optical frequency.

Estimates of the antenna properties above for the ridge OMA are provided in table 1. We assume an effective antenna length of 2 mm limited by dephasing. The field of view is from θ of 35° to 79°. We compute the optical bandwidth around $\theta = 60°$ with an optical group index of 4.3 and a mechanical group velocity of 4135 m/s.

6. Nonreciprocity and multiplexing mechanics

In addition to two-dimensional beam-steering, active gratings generated by mechanical waves naturally implement certain functionalities that are not intrinsically present in other approaches.

First, the time-varying grating generated by a unidirectional mechanical field breaks reciprocity in the structure. Therefore the system operates as a nonreciprocal metasurface [38]: light that is scattered out is shifted up in frequency by Ω and the light coming back is shifted up *again* in frequency by Ω such that the roundtrip optical frequency shift is 2Ω [Fig. 4]. Therefore the system naturally includes a frequency-shifting function that can be used for heterodyning with an on-chip local oscillator.

Second, even at a fixed optical wavelength we can inject a superposition of mechanical waves with different wavevectors. Each of these mechanical waves generates an outgoing beam at a separate angle that can be controlled, sent to different targets, and read out independently

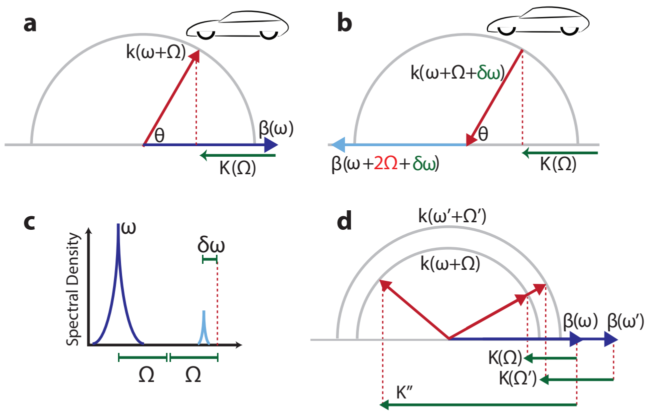

Fig. 4. (a) On the transmit side, the optical wave at ω is shifted to an outgoing optical wave at frequency $\omega + \Omega$. (b) The backscattered light now has an additional Doppler shift of $\delta\omega$. This incoming wave mixes with the same mechanical wave and excites the optical waveguide at frequency $\omega + 2\Omega + \delta\omega$. (c) The resulting optical spectrum allows us to distinguish between light being sent and received, moving the received beam outside of the laser phase noise. (d) The outgoing radiation can be multiplexed dynamically by exciting a superposition of mechanical waves. Each of the outgoing beams can be controlled independently. As a special case, this implies widely different optical wavelengths can be sent to and received from the same spot.

[Fig. 4(d)]. As a special case, this enables multiple optical wavelengths to be sent to and received from a single angular spot. Such functionality may prove useful in the realization of free-space communication links [11,39], (holographic) video displays [14,40], remote sensing [41–43], and coherent imaging [44,45].

7. Conclusion

In conclusion, we propose an on-chip, two-dimensional beam-steering system compatible with standard microelectronics processes based on guided mechanical waves. We design hybrid photonic-phononic waveguides whose mechanical excitations can travel on the surface of a silicon-on-insulator chip. The propagating mechanical fields – acting as active gratings – convert between guided and radiating optical fields in a rapidly reconfigurable way. Efficient optical mode conversion can be realized in millimeter-scale apertures with low mechanical drive power. The system can steer monochromatic light over a large field of view; distinguish between outgoing and incoming light through a nonreciprocal frequency shift; and control the beam direction, beam shape, and the number of beams. More generally, we have shown that subwavelength control of photons and phonons enables low-power, dynamic control of light.

Appendix A Simulation methods

A.1 Nonperturbative method of computing scattering rates

We perform nonperturbative scattering simulations with the finite-element solver COMSOL [46] solving Maxwell's equations in either 2D or 3D in the frequency domain. The resulting eigenvalue problem has nearly guided solutions. Light scattered out of the slab is absorbed by a perfectly matched layer, causing the eigenvalue to become complex $\omega \longrightarrow \omega - i\frac{\kappa}{2}$. In this section we show that the scattering rate α is related to κ as

$$\alpha = \frac{\kappa}{v_g} = \frac{\omega}{Q v_g} \tag{10}$$

where $v_g = c/n_g$ is the optical group velocity.

Consider an optical waveguide with energy per unit length $\mathcal{E}$, power transmitted down the waveguide $\mathcal{P}$, and power scattered out of the waveguide per unit length $\mathcal{P}_s$. We would like to relate $\mathcal{P}_s$ to the attenuation rate α. Energy conservation yields

$$\partial_t \mathcal{E} = -\partial_z \mathcal{P} - \mathcal{P}_s \tag{11}$$

which for steady state $\partial_t \to 0$ becomes $\partial_z \mathcal{P} = -\mathcal{P}_s$. Since

$$Q = \frac{\omega}{\kappa} \quad \text{and} \quad \kappa = \frac{\mathcal{P}_s}{\mathcal{E}}, \tag{12}$$

our statement of energy conservation becomes

$$\partial_z \mathcal{P} = -\frac{\omega}{Q}\mathcal{E} \tag{13}$$

which can be reexpressed using $v_g = \frac{\mathcal{P}}{\mathcal{E}}$ as

$$\partial_z \mathcal{P} = -\underbrace{\frac{\omega}{Q v_g}}_{\equiv\alpha} \mathcal{P}. \tag{14}$$

Therefore, the optical power decays exponentially at a rate α that can be expressed in terms of the imaginary part of the eigenvalues of our numerical solutions.

A.2 Verification of the model

A.2.1 Literature grating simulation

We test our nonperturbative computational approach by modeling two wavelength-scale periodic optical structures from the literature: (1) a high index-contrast, strong silicon-on-insulator grating coupler [47] used in imec's silicon photonics pilot line [48] and (2) a low index-contrast, weak grating coupler [49].

Table 3. **References [47] and [49] provide the scattering rate α as a function u for these gratings. We compute α_m by estimating a couple of points in their figures in a similar range of u. Our model agrees with the literature result up to 3% for the strong grating and up to 5.6% for the weak grating.**

	α_m (mm^{-1}nm^{-2})	α_m^{-1}(mm nm^2)
SOI literature [47,48]	0.059	16.9
Our model	0.061	16.4
Little [49]	$7.5 \cdot 10^{-4}$	1333
Our model	$7.1 \cdot 10^{-4}$	1408

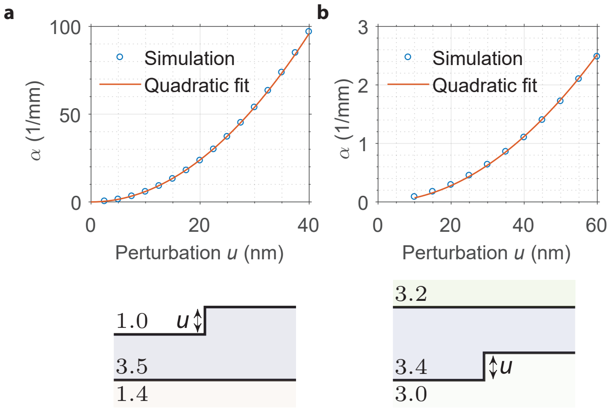

Fig. 5. We compute scattering rates for strong and weak gratings previously demonstrated to verify our numerical methods. The scattering strength scales quadratically with the perturbation u. (a) Simulation of a strong SOI grating [47] that has been tested experimentally [47, 48]. The group index of the optical mode is $n_g = 3.6$ and the Bloch index is 2.85. The grating pitch is 630 nm and the core thickness is 220 nm. (b) Simulation of a weak grating [49]. The group index of the optical mode is $n_g = 3.4$ and the Bloch index is 3.29. The grating pitch is 10 μm and the core thickness is 500 nm.

A.2.2 PML tests

We implement the perfectly matched layers (PMLs) at the bottom and top of the simulation as an imaginary part of the refractive index $\Im n$ starting a distance $x_{\text{start}} = 6\ \mu$m above and below the waveguide. For $|x| > x_{\text{start}}$ the strength of the PML is set by

$$\Im n = \left(\frac{|x| - x_{\text{start}}}{x_{\text{pml}}} \right)^2 \tag{15}$$

such that $\Im n = 1$ at a distance $|x| = x_{\text{start}} + x_{\text{pml}} = 15\ \mu$m away from the waveguide. The computational domain ends at $|x| = x_{\text{end}} = \frac{d}{2} + 20\ \mu$m with perfectly conducting boundaries and $d = 220$ nm the typical core thickness. We set the maximum mesh size in the core and free-space domains at 10 nm and 150 nm. With these parameters, the simulation time is about 20 s for a wavelength of 0.63 μm. We check PML operation with the following tests, all for the SOI grating coupler of Fig. 5(a) and for a perturbation of $u = 5$ nm. The scattering rate $\alpha \approx 1.42/\text{mm}$ in these tests [Fig. 5(a) and 6].

First, we investigate the field intensity in the free-space domain. For $1\ \mu\text{m} < |x| < x_{\text{start}}$ the field remains roughly constant, confirming that the PML mainly measures the radiation power and not the evanescent field of the guided mode. Next, we sweep the size of the computational domain x_{end} [Fig. 6(a)]. The scattering rate saturates fast, likely because of reduced reflections off the perfectly conducting boundaries, and stays constant up to 10^{-4} fractionally afterwards. Second, we sweep x_{pml} and thus the PML strength [Fig. 6(b)]. The scattering rate decreases rapidly until $x_{\text{pml}} > 2\ \mu$m and then fluctuates at 10^{-4} fractionally. Third, we sweep x_{start} and $x_{\text{pml}} = x_{\text{start}} + 3\ \mu$m while keeping other parameters constant [Fig. 6(c)]. The scattering rate oscillates initially and then stays constant up to 10^{-4} fractionally. Fourth, we sweep the maximum mesh element size in the free-space domains [Fig. 6(c)]. The scattering rate again fluctuates at 10^{-4} level fractionally.

Our standard operating parameters are all chosen in these regions of 10^{-4} fractional sensitivity to discretization and PML parameters. Therefore, we expect simulation results accurate at

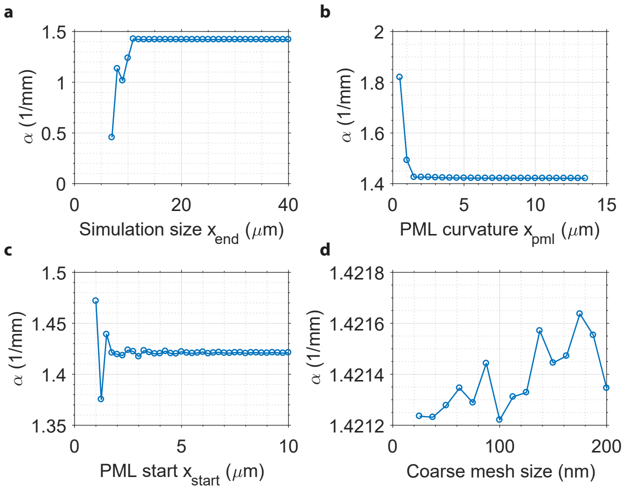

Fig. 6. The scattering rate is insensitive to changes in the PML. (a) A sweep of simulation size x_{end} shows initially an increase and then saturation of the scattering rate α when $x_{\text{end}} > 10\,\mu$m. (b) The scattering rate drops fast with PML curvature x_{pml} and saturates beyond $x_{\text{pml}} > 2\,\mu$m. (c) The scattering rate remains constant when $x_{\text{start}} > 3\,\mu$m. (d) Coarse mesh size does not strongly impact scattering rate below 200 nm. Similarly, the fine mesh size does not affect the scattering rate below 20 nm.

percent-level at least for decay rates far above $\frac{\kappa}{2\pi} \approx 10$ MHz, quality factors below $Q \approx 10^7$, scattering rates above $\alpha \approx 10$/m and decay lengths below $\alpha^{-1} \approx 10$ cm. We determine all scattering rates a factor 10^3 to 10^4 away from these thresholds. The quadratic scaling of scattering rate with respect to perturbations enables extrapolation to smaller perturbations u where necessary.

A.2.3 FDTD calculations

In addition to the COMSOL-based frequency-domain models, we also developed Lumerical-based finite-difference time-domain (FDTD) [50] 2D and 3D models to compute the scattering rates and radiation patterns. Here we inject a pulse with a bandwidth of 5 to 10 nm and determine the scattering rate α from the exponential decay of the guided power. Lumerical has built-in functions that allow for a straightforward determination of the electromagnetic beam in the far-field and thus the angles and strengths of the first-, second- and higher-order grating lobes. The results generally agree with the COMSOL-based frequency-domain approach described above and in the main text. We focus on the faster frequency-domain simulations.

Appendix B Silicon slab in air with sinusoidal perturbation

B.1 Scattering rate comparison

In this section, we investigate the scattering rates of suspended silicon-on-insulator slabs in greater detail.

Table 4 shows a comparison of the scattering rates of five types of perturbations to a 220 nm thick silicon slab waveguide. We perform these calculations at fixed frequency of 193.5 THz and fixed scattering angle of 67°. The Bloch index of the optical slab mode is about 2.82 and the grating pitch is 630 nm. From top to bottom, the first grating is the silicon-on-insulator grating of section A.2.1. It has only a top surface rectangular perturbation. The second grating has air both above and below the core. Its scattering rate is slightly higher owing to the increased

Table 4. **The scattering rate varies several orders of magnitude depending on the type of perturbation. A symmetric, sinusoidal perturbation has the largest scattering rate in a** 220 **nm thick silicon slab. For some perturbations the scattering rate scales with** u^4 **instead of** u^2 **because of destructive cancellations in the term proportional** u^2**. In general the scattering rate contains all terms** u^{2l} **with** l **any positive integer. Here we use the perturbation-normalized quality factor as** $Q_\mathrm{m} = \omega/(\alpha_\mathrm{m} v_\mathrm{g})$**.**

	α_m (mm^{-1}nm^{-2})	α_m^{-1}(mm nm^2)	Q_m (nm^2)
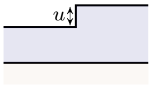	0.059	16.9	$2.5 \cdot 10^5$
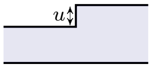	0.073	13.7	$2.0 \cdot 10^5$
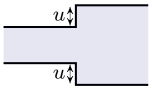	$1.4 \cdot 10^{-6}\,(u(\mathrm{nm}))^2$	$\frac{7.1 \cdot 10^5}{(u(\mathrm{nm}))^2}$	$\frac{10^{10}}{(u(\mathrm{nm}))^2}$
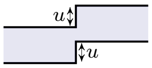	0.31	3.2	$5.8 \cdot 10^4$
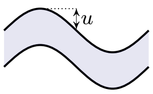	0.74	1.3	$2.4 \cdot 10^4$

index-contrast. The third structure has a symmetric perturbation to the top and bottom surfaces. Its scattering rate for a $\delta = 1$ nm perturbation is about four orders of magnitude below that of the SOI grating coupler that breaks vertical symmetry. In addition, its scattering rate scales with δ^4 instead of the usual δ^2 – even though second-order scattering (satisfying $\beta - 2K = k \cos\theta_\mathrm{2nd}$) is not phase-matched for any angle θ_2nd when $\theta = 67°$. The suppressed scattering and δ^4-scaling arise from destructive cancellations in the fields scattered from the top and bottom surfaces, see Fig. 7 and discussion below for details. The fourth grating is identical except in that it has an antisymmetric perturbation to the top and bottom surfaces. The scattering rate α is a factor $\frac{0.31}{0.073} = 4.3$ larger than that of a grating with a perturbation only on the top surface. The enhanced scattering arises from constructive interference between the fields radiated by top and bottom perturbations [Fig. 7]. The fifth grating has a sinusoidal instead of a rectangular perturbation. It is nearly identical to the dynamic mechanical field we propose to excite. The first Fourier component of a rectangular signal is $\frac{2}{\pi}$, so the scattering by the sinusoidal perturbation is a factor $(\pi/2)^2 = 2.4$ stronger. The sinusoidal symmetric perturbation to a 220 nm-thick suspended silicon slab thus has an overall enhancement of a factor 10.2 with respect to grating coupler with air below and a factor 12.5 compared to a typical silicon-on-insulator grating coupler.

B.2 Thickness dependence of scattering rate

Next, we compute the scattering rate as a function of waveguide thickness for sinusoidal symmetric and antisymmetric perturbations [Fig. 7] for the same parameters as in subsection B.1. We find the scattering rate α for the antisymmetric perturbation to be maximal when

$$d = \left(l + \frac{1}{2}\right) \lambda_\mathrm{Si} \tag{16}$$

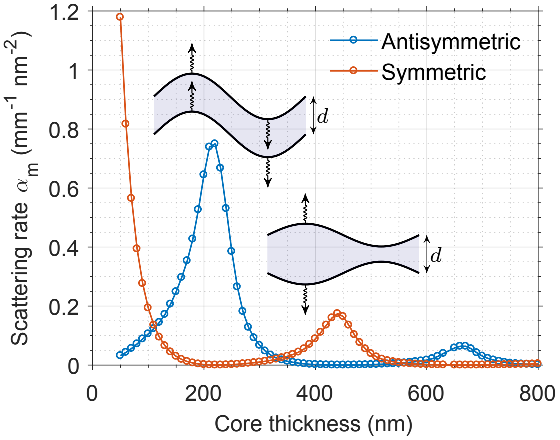

Fig. 7. The scattering rate α_{m} caused by the antisymmetric sinusoidal perturbation is maximal at thicknesses $d = \left(l + \frac{1}{2}\right)\lambda_{\mathrm{Si}}$ with $\lambda_{\mathrm{Si}} = \frac{\lambda}{n_{\mathrm{Si}}} = 443\,\mathrm{nm}$ the optical wavelength in silicon and l a positive integer, while it vanishes at $d = l\lambda_{\mathrm{Si}}$. A symmetric sinusoidal perturbation yields the opposite behavior. This behavior is caused by interference between the scattered field from the top surface and that scattered from the bottom surface. As the waveguide core becomes thicker, the structure is less sensitive to either type of perturbation. One simulation point just above a thickness of 600 nm was removed manually as the script had selected the wrong optical mode. We computed both curves for a perturbation $u = 10\,\mathrm{nm}$.

with d the core thickness, l an integer and $\lambda_{\mathrm{Si}} = \frac{\lambda}{n_{\mathrm{Si}}} = 443\,\mathrm{nm}$ the optical wavelength in silicon. The scattering vanishes when

$$d = l\lambda_{\mathrm{Si}} \tag{17}$$

while the core with a symmetric perturbation exhibits the reverse behavior. The effect arises from interference between the scattered fields generated by the top and bottom slab surfaces. For an antisymmetric perturbation, there is another 180° shift in the phasing of the top and bottom scatterers. Therefore, constructive interference occurs when the thickness is a multiple of a wavelength plus an additional half-wavelength to compensate for the 180° phasing of the sources. Interestingly, the global maximum in the scattering rate of an antisymmetric perturbation – similar to that of a Lamb-type mechanical field – occurs exactly at a core thickness of $d = 220\,\mathrm{nm}$. In addition, this antisymmetric sinusoidal perturbation offers the strongest scattering rates of all the perturbation types (table 4). Hence antisymmetric Lamb-like flexural mechanical fields propagating along a 220 nm-thick suspended silicon waveguide are ideal excitations for coupling guided and free-space optical fields.

B.3 Photoelasticity

Even in absence of a geometric boundary perturbation, a propagating mechanical wave generates an inohomogeneous strain profile that couples guided optical fields to radiating fields. This is termed the photoelastic contribution α_{pe} to the total scattering rate α_{tot}. The scattering rates reported above include only the boundary-induced scattering α_{mb}. Generally speaking, the two contributions may be of similar size and thus interfere with one another – either enhancing the total scattering rate or potentially completely canceling it [18, 23, 51]. However, in a simulation without the boundary perturbation our eigenfrequency model predicts a photoelastic scattering rate of $\alpha_{\mathrm{pe}} = 1.4 \cdot 10^{-2}/(\mathrm{mm\,nm}^2)$ – nearly two orders of magnitude smaller than $\alpha_{\mathrm{mb}} = 0.74/(\mathrm{mm\,nm}^2)$ (table 4) for a suspended 220 nm-thick silicon slab. Thus the photoelastic component of the scattering is weak in the considered geometry: even in case of completely destructive or constructive interference the total scattering rate

$$\frac{\alpha_{\text{tot}}}{\alpha_{\text{mb}}} = \left(1 \mp \sqrt{\frac{\alpha_{\text{pe}}}{\alpha_{\text{mb}}}}\right)^2 = 1^{+0.29}_{-0.26} \tag{18}$$

would change by less than 30%. Next, we simulate the combined scattering rate resulting from interference between the moving-boundary and photoelastic scattering. We find that the two effects interfere constructively such that $\alpha_{\text{tot}} = 0.96/(\text{mm}\,\text{nm}^2)$ – about 30% larger than α_{mb}.

In this computation of α_{pe} and α_{tot} we implemented the photoelasticity as an anisotropic refractive index profile with components

$$n_{\text{core}} = \begin{pmatrix} n_{\text{Si}} + \Delta n_{xx} & 0 & \Delta n_{xz} \\ 0 & n_{\text{Si}} + \Delta n_{yy} & 0 \\ \Delta n_{xz} & 0 & n_{\text{Si}} + \Delta n_{zz} \end{pmatrix} \tag{19}$$

where the index variations Δn are given by

$$\Delta n_{xx} = -\frac{1}{2} n_{\text{Si}}^3 p_{12} S_{zz} \tag{20}$$

$$\Delta n_{yy} = -\frac{1}{2} n_{\text{Si}}^3 p_{12} S_{zz} \tag{21}$$

$$\Delta n_{zz} = -\frac{1}{2} n_{\text{Si}}^3 p_{11} S_{zz} \tag{22}$$

$$\Delta n_{xz} = -n_{\text{Si}}^3 p_{44} S_{xz} \tag{23}$$

with $(p_{11}, p_{12}, p_{44}) = (-0.09, 0.017, -0.051)$ the photoelastic tensor of silicon assuming waveguide orientation along a $\langle 100 \rangle$ axis. The waveguide orientation has a minor effect on the effective photoelastic components in silicon. The strain components are given by

$$S_{zz} = \partial_z u_z = -K^2 x u \sin Kz \tag{24}$$

$$\begin{aligned} S_{xz} &= \frac{1}{2}\left(\partial_z u_x + \partial_x u_z\right) \\ &= S_{zx} = 0 \end{aligned} \tag{25}$$

where K is the mechanical wavevector, u the maximum mechanical perturbation and $(u_x, u_z) = u(\sin Kz, -Kx\cos Kz)$ a snapshot of the displacement field of an antisymmetric Lamb-wave propagating along a thin slab opposite to the z-direction. The origin of the transverse coordinate x is taken to be in the center of the slab, such that $|x| = d/2$ corresponds to the silicon/air interfaces with d the slab thickness. This analytical Lamb-wave solution assumes $Kd \ll 1$. Finite-element simulations showed that the actual mechanical field around $Kd \approx 1$ is still captured well by this analytical approximation. In these simulations we swept u and then obtained α_{pe} and α_{tot} from a fit to u^2 as in Fig. 5.

In general a full 3D simulation of the combined effects of moving boundaries and photoelasticity must be developed and is possible in our eigenfrequency approach. We have however limited our current 3D simulations to the moving-boundary effect given the expected weakness of photoelasticity in this system. We suspect that this weakness is caused by the distributed nature of the photoelastic scattering, leading to destructive interferences in the outgoing radiation similar to Fig. 7.

Appendix C Perturbation theory for optomechanical antennas

In cavity optomechanics and Brillouin scattering, the optomechanical interaction is described perturbatively by expanding the permittivity in terms of the mechanical deformation

$$\varepsilon \rightarrow \varepsilon + \delta_u \varepsilon \cdot \mathbf{u} + O\left(\mathbf{u}^2\right). \tag{26}$$

We can take the same approach to describe scattering out of a waveguide. After a Fourier transform $\partial_t \rightarrow -i\omega$, Maxwell's equations for the electric field reduce to

$$\left(\nabla \times \nabla \times - \mu\varepsilon\omega^2\right)\mathbf{E} = i\omega\mu\mathbf{J} \tag{27}$$

where $\mathbf{J}$ is a current density. We are interested in a current-free waveguide with a mechanically perturbed permittivty

$$\underbrace{\left(\nabla \times \nabla \times - \mu\varepsilon\omega^2\right)}_{\mathbf{\Theta}}\mathbf{E} = \mu\omega^2\left(\delta_u \varepsilon \cdot \mathbf{u}\right)\mathbf{E}. \tag{28}$$

We first solve the uncoupled equations – Maxwell's and the theory of elasticity – for the optical and mechanical modes of the waveguide. The unperturbed electric field satisfies $\mathbf{\Theta E} = 0$, which can be rewritten as a generalized eigenvalue problem of the form $\mathbf{AE} = \omega^2\mathbf{BE}$ with Hermitian operators $\mathbf{A}$ and $\mathbf{B}$. Expanding $\mathbf{E} \rightarrow \mathbf{E} + \mathbf{E}_\mathrm{r} + \ldots$ and $\omega^2 \rightarrow \omega^2 + \omega_1^2 + \ldots$ the perturbed field is given by

$$\mathbf{\Theta E}_\mathrm{r} = \mu\varepsilon\omega_1^2\mathbf{E} + \mu\omega^2\left(\delta_u \varepsilon \cdot \mathbf{u}\right)\mathbf{E} \tag{29}$$

to first order in $\mathbf{u}$. Since $\mathbf{\Theta}$ is Hermitian, $\mathbf{\Theta}|\mathbf{E}\rangle = 0$ implies that $\langle\mathbf{E}|\mathbf{\Theta}|\mathbf{E}_\mathrm{r}\rangle = 0$. Taking the inner product with $|\mathbf{E}\rangle$ on both sides yields the first order correction to the eigenvalue

$$\omega_1 = -\frac{\omega}{2}\frac{\langle\mathbf{E}|\delta_u\varepsilon \cdot \mathbf{u}|\mathbf{E}\rangle}{\langle\mathbf{E}|\varepsilon|\mathbf{E}\rangle} \tag{30}$$

where we've adopted Dirac notation and substituted $\omega_1^2 \rightarrow 2\omega\omega_1$. For proper choice of inner product and normalization of $\mathbf{u}$, ω_1 becomes the coupling rate of cavity optomechanics g_0 or Brillouin scattering $\tilde{g}_0$ [21,52,53].

We can express the outgoing field fully in terms of $\mathbf{\Theta}$ and the unperturbed fields

$$\mathbf{\Theta E}_\mathrm{r} = \mu\omega^2\left(\delta_u \varepsilon \cdot \mathbf{u}\right)\mathbf{E}. \tag{31}$$

The optomechanical interaction above can be expressed in terms of a current

$$\mathbf{J}_\mathrm{om} = -i\omega\left(\delta_u \varepsilon \cdot \mathbf{u}\right)\mathbf{E} \tag{32}$$

allowing us to rewrite the remaining inhomogeneous equations simply as

$$\mathbf{\Theta E}_\mathrm{r} = i\omega\mu\mathbf{J}_\mathrm{om}. \tag{33}$$

C.1 The moving-boundary and photoelastic effect

Next we present an explicit expression for the nonlinear polarization current $\mathbf{J}_\mathrm{om}$. Mechanical waves give rise to changes in the permittivity ε which can be expressed to first order in $\mathbf{u}$ in terms of body (*i.e.* photoelastic effect [54]) and boundary contributions. The latter requires careful handling to manage discontinuities in the field at boundaries of dielectrics treated by Johnson *et al.* [52,55]. This variation in the permittivity $\delta_u\varepsilon \cdot \mathbf{u}$, which is familiar in the fields of cavity optomechanics and Brillouin scattering, is here a tensor which acts on $\mathbf{E}$ to give the polarization currents $\mathbf{J}_\mathrm{om}$ above.

Consider a domain Ω with boundary $\partial\Omega$ deformed by $\mathbf{u}$. The normal $\mathbf{n}$ points out of the domain such that for positive $\mathbf{u}\cdot\mathbf{n}$ the permittivity of a region in the neighborhood of the boundary changes by $\Delta\varepsilon \equiv \varepsilon_{\text{in}} - \varepsilon_{\text{out}}$. The main trick in forming a well-defined expression for the radiation pressure on the boundary is to avoid field discontinuities by replacing the component of $\mathbf{E}$ normal to $\partial\Omega$ with the electric displacement field $\mathbf{D}$. The boundary contribution then becomes

$$\delta_u \varepsilon_{\text{rp}} \cdot \mathbf{u} = (\mathbf{u}\cdot\mathbf{n})\,\delta_{\partial\Omega}\left(\Delta\varepsilon \mathbf{\Pi}_{\parallel} - \varepsilon\Delta\varepsilon^{-1}\varepsilon\mathbf{\Pi}_{\perp}\right) \tag{34}$$

which is expressed in terms of the tensors $\mathbf{\Pi}_{\parallel}$ and $\mathbf{\Pi}_{\perp} = \mathbb{I} - \mathbf{\Pi}_{\parallel}$ which project the electric field into the plane of the dielectric interface or along the normal $\mathbf{n}$, respectively. Here $\Delta\varepsilon^{-1} \equiv \varepsilon_{\text{in}}^{-1} - \varepsilon_{\text{out}}^{-1}$ and the delta function on the boundary $\delta_{\partial\Omega}$ renders $(\delta_u\varepsilon\cdot\mathbf{u})\,\mathbf{E}$ into a surface current on $\partial\Omega$.

Suppose the normal is oriented in Cartesian coordinates along $\mathbf{z}$ and the dielectric boundary is at $z = 0$. Then

$$\left(\delta_u \varepsilon_{\text{rp}} \cdot \mathbf{u}\right)\mathbf{E} = u_z \delta(z)\begin{bmatrix}\Delta\varepsilon E_x \\ \Delta\varepsilon E_y \\ -\varepsilon\Delta\varepsilon^{-1}D_z\end{bmatrix}. \tag{35}$$

The $\mathbf{z}$ component of the expression above poses some difficulty as ε is discontinuous as $z = 0$. This is discussed in the next section.

Although in this work estimates of the photoelastic effect justified dropping it from our calculations, we give its contribution to the variation of ε below for completeness. The photoelastic tensor in common use is defined such that a strain $\mathbf{S}$ causes $\varepsilon\Delta\varepsilon_{ij}^{-1} = (\mathbf{pS})_{ij} = p_{ijkl}S_{kl}$. To first order in $\mathbf{u}$,

$$\delta_u \varepsilon_{\text{pe}} \cdot \mathbf{u} = -\varepsilon\frac{\mathbf{pS}}{\varepsilon}\varepsilon. \tag{36}$$

C.2 Implementing the boundary contribution to J_{om}

The boundary contribution to the scattering process is delta-distributed across the boundary. In the plane of a dielectric interface – along the $\mathbf{x}$ and $\mathbf{y}$ axis in Eq. (35) – the perturbation behaves like a surface current giving rise to discontinuities in the magnetic field

$$\mathbf{n}\times\Delta\mathbf{H} = \mathbf{J}_{\parallel}. \tag{37}$$

The $J_{\perp}$ component of the surface current isn't implemented as a set of boundary conditions. Instead $J_{\perp}$ is taken to be a uniform volume current density of finite thickness $t_J = 5$ nm just inside the boundaries of our silicon waveguides, normalized by the thickness so as to converge to a delta function the limit $t_J \to 0$.

The expression for $J_{\perp}$ is the product of a step and a delta function at the boundary, and volume approximations of the delta function therefore require some choice of ε in the $\mathbf{z}$ component of Eq. (35). Although $J_{\perp}$ is discontinuous, the power sourced into the field $-\mathbf{E}\cdot\mathbf{J}_{\text{om}}$ *is* continuous, making the radiated field robust to the exact distribution used for $J_{\perp}$ [55].

We check our implementation of $J_{\perp}$ by computing the OM radiation of the fundamental TM modes of 220 nm, 340 nm, and 440 nm silicon slab waveguides both perturbatively and nonperturbatively. The results are displayed in Fig. 8.

Appendix D Geometric disorder and dephasing

Geometric disorder has been studied extensively in nanophotonic circuits [29,31,32,56–58] to understand optical propagation losses. It has also been investigated in the context of Brillouin scattering – where it leads to broadening of the mechanical resonance [18,19,23,59]. In both cases the standard deviation of geometric disorder was generally estimated at $\sigma \approx 1$ nm with

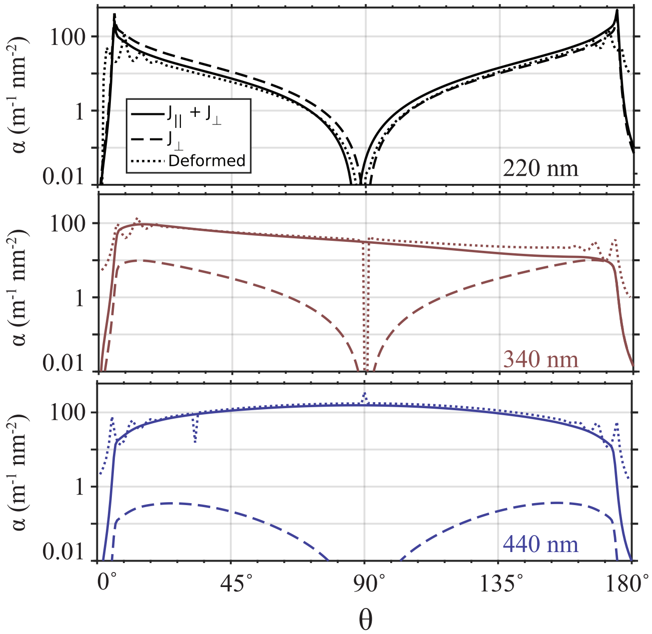

Fig. 8. The scattering rates α are computed for, from top to bottom, a 220 nm, 340 nm, and 440 nm slab with and without the volume current used to implement the $J_\perp \propto D_z$ component of the boundary interaction. For the 220 nm slab, the $J_\perp$ term dominates and our perturbative (dashed) and nonperturbative (dotted) calculations agree well.

the largest disorder occurring near etched sidewalls. In studies focusing on optical scattering losses, the coherence lengths ξ were found to be below 100 nm [31, 57]. Such short coherence lengths are not consistent with (1) wafer-scale geometric disorder [56], (2) millimeter-scale optical dephasing lengths [58] nor with (3) the Brillouin resonance broadening observed in silicon waveguides [18, 23, 59]. Therefore, we suspect the spatial correlator to contain at least two terms: (1) a fast-disorder term with a coherence length of about 50 nm and (2) a slow-disorder term with a coherence length of about 50 μm. The fast roughness mainly determines optical radiation loss and backscatter – both of which require large roughness momentum – while the slow drift mainly determines the dephasing as it builds up over many wavelengths. We expect slow disorder to be the main hurdle for the proposed device and thus tabulate the various sensitivities in the main text using $\xi \approx 50\,\mu$m.

In the main text, we provided the results of our analysis of dephasing. Here we discuss the derivations in detail. There are eight cases to be investigated: the out- vs. incoupling, anti-Stokes vs. Stokes and counter- vs. copropagating cases could each be combined. Four of these cases suffer from low efficiencies due to a large phase-mismatch. The remaining four cases are (1) outcoupling by anti-Stokes scattering between counter-propagating guided waves, (2) outcoupling by Stokes scattering between copropagating guided waves, (3) incoupling by Stokes scattering between copropagating guided waves and (4) incoupling by anti-Stokes scattering between counter-propagating guided waves. Cases (3) and (4) are the time-reversed versions of cases (1) and (2) respectively. Thus they have identical properties and we limit ourselves to cases (1) and (2) in the following.

Case (1) is attractive as it allows for optical and mechanical excitation from opposite sides of the array. In anti-Stokes scattering phase errors of the guided optical and the guided mechanical wave add, yielding a total phase error of

$$\delta\varphi(z) = \int_0^z dz'\,\delta\beta(z') - \int_L^z dz'\,\delta K(z') \tag{38}$$

The optical phase error grows forwards while the mechanical phase error grows backwards. The variance of the phase error is

$$\begin{aligned}\langle\delta\varphi^2(z)\rangle = &\int_0^z\int_0^z dz'dz''\,\langle\delta\beta(z')\delta\beta(z'')\rangle\\ &+\int_L^z\int_L^z dz'dz''\langle\delta K(z')\delta K(z'')\rangle\\ &+2\int_0^z\int_z^L dz'dz''\,\langle\delta\beta(z')\delta K(z'')\rangle.\end{aligned} \tag{39}$$

To compute these terms, we expand $\delta\beta = \sum_l \partial_l\beta\delta X_l$ and $\delta K = \sum_l \partial_l K\delta X_l$ and assume a spatial correlator for the disorder

$$\langle\delta X_l\,(\Delta z)\,\delta X_l\,(0)\rangle = \sigma_l^2 e^{-|\Delta z|/\xi_l}. \tag{40}$$

With this explicit form for the noise correlator, the first term becomes

$$\begin{aligned}\int_0^z\int_0^z \mathrm{d}z''\mathrm{d}z'\,e^{-|\Delta z|/\xi_l} &= 2\xi_l\left(z-\xi_l+\xi_l e^{-z/\xi_l}\right)\\ &\overset{z\gg\xi_l}{\approx} 2\xi_l z\end{aligned} \tag{41}$$

with $\Delta z = z' - z''$ and similarly for the δK-term. For $z \gg \xi_l$ and $L - z \gg \xi_l$ the $\delta\beta\delta K$ cross-term in Eq. (39) is negligible. Substituting Eq. (41) into Eq. (39) we find

$$\left\langle\delta\varphi^2\,(z)\right\rangle = \sum_l 2\partial_l\beta^2\sigma_l^2\xi_l z + 2\partial_l K^2\sigma_l^2\xi_l\,(L-z)\,. \tag{42}$$

Above we relied on an explicit form for the correlator and simplified the result in the limit where $z \gg \xi_l$. In this limit a more general expression for $\left\langle\delta\varphi^2\,(z)\right\rangle$ can be derived in terms of the power spectral density of the disorder $S_{\eta\eta}$ for noise process η. As a result of the central limit theorem, any stationary noise process of finite variance integrated over lengths greater than the noise's correlation length is Gaussian-distributed. The variance of this integrated process equals the product of $S_{\eta\eta}[0]$ and the propagation length [60]. For example fluctuations $\delta\beta$ in the optical wave vector are integrated over the length of the waveguide z contributing to the phase error $\delta\varphi$ as a Gaussian with variance $S_{\beta\beta}[0]z$. Here the power spectral density $S_{\beta\beta}[\omega]$ of $\delta\beta$ is

$$S_{\beta\beta}[\omega] = \int_{-\infty}^{+\infty} dz\,e^{i\omega z}\langle\delta\beta(z)\delta\beta(0)\rangle. \tag{43}$$

Again dropping the $\delta\beta\delta K$ crossterm, it follows that

$$\left\langle\delta\varphi^2\,(z)\right\rangle = S_{\beta\beta}[0]z + S_{KK}[0](L-z) \tag{44}$$

as reported in section 5.

We can check that Eq. (42) and Eq. (44) match. The power spectrum for Eq. (40) is

$$S_{\beta\beta}[\omega] = \sum_l \frac{2(\partial_l\beta\sigma_l)^2\xi_l}{1+(\omega\xi_l)^2}. \tag{45}$$

If we plug this expression at $\omega = 0$ and the corresponding one for δK into Eq. (44) we find Eq. (42).

In case (2), Stokes scattering implies that the guided optical and guided mechanical phases subtract such that

$$\delta\varphi(z) = \int_0^z dz' \, \delta k_{\shortparallel} \tag{46}$$

with $k_{\shortparallel} = \beta - K$ so one can show as in the above that

$$\langle \delta\varphi^2(z) \rangle = S_{k_{||}k_{||}}[0] z \tag{47}$$

The thermal dephasing lengths in the main text were derived along similar lines but with constant $\delta\beta$ and δK along the antennas.

Appendix E Mechanical losses

Material losses cause mechanical waves to decay at a rate $\gamma = \Omega/(Q_{\mathrm{m}} v_{\mathrm{m}})$ where Q_{m} is the mechanical quality factor and v_{m} is the mechanical group velocity. At room temperature, nonlinear phonon processes limit mechanical Qs of silicon resonators to $Q \approx 10^4$ [61]. Waves in the ridge OMA presented in the text at $K = 2\pi \times 1.2\ \mu\mathrm{m}^{-1}$ which scatters light at $\theta = 60°$ have a frequency $\Omega = 2\pi \times 3.42$ GHz and group velocity $v_{\mathrm{m}} = 4135$ m/s. Assuming a quality factor $Q_{\mathrm{m}} = 3 \times 10^3$, the resulting decay length is $\gamma^{-1} = 580\ \mu$m.

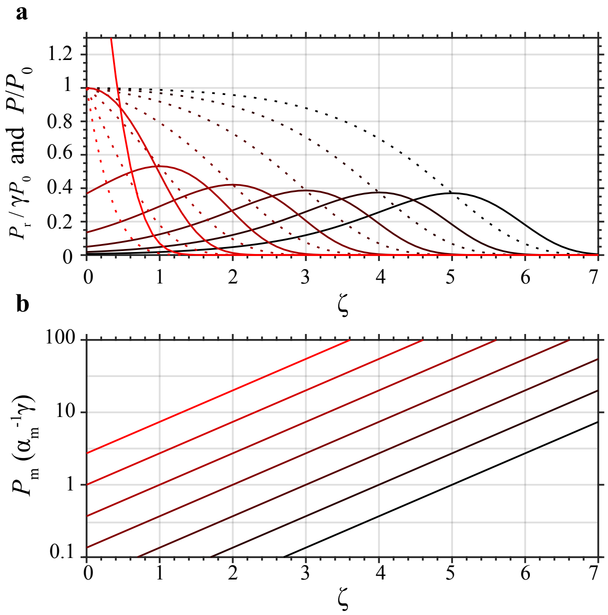

Fig. 9. Mechanical losses alter the exponential envelope of an ideal OMA, limiting the effective aperture and increasing the mechanical power needed to achieve it. (a) The solid curves show power radiated per unit length across an antenna for values of $\zeta_{\max} = -\log a$ ranging from -1 to 5 (from red-to-black in even steps). Large scatterings rates a results in approximately exponential radiation patterns as in the lossless case. As a decreases, the profile shifts toward higher z with a constant FWHM of $\Delta\zeta = 2.45$. The dotted curves show the fraction of the guided light remaining in the waveguide, plotted on the same axes. (b) The mechanical power needed to achieve a particular radiation pattern is plotted against the antenna's length L on the same abscissa as (a).

Attenuation of the mechanical waves modifies the optical scattering rate α from the antenna and thereby the radiation pattern of an OMA. Consider the counter-propagating optical and mechanical waves of the anti-Stokes process for which

$$\partial_z \mathcal{P} = -\alpha_{\mathrm{m}} \mathcal{P}_{\mathrm{m}} \mathcal{P} \tag{48}$$

$$\partial_z \mathcal{P}_{\mathrm{m}} = \gamma \mathcal{P}_{\mathrm{m}} \tag{49}$$

where α_{m} is a power-normalized scattering rate, not to be confused with the displacement-normalized rate represented by α_{m} in the rest of the text. In the above equations we assume the mechanical drive $\mathcal{P}_{\mathrm{m}}$ is undepleted by the scattering process, a reasonable assumption since the phonon flux for a 1 mW drive is larger than a 1 mW optical guided wave by a factor of $\omega/\Omega \approx 10^5$. The optical power is $\mathcal{P}_0$ at the beginning of the antenna where $z = 0$ and the mechanical power is $\mathcal{P}_{\mathrm{m}\,0}$ at the end of the antenna where $z = L$. We can solve these equations given the boundary conditions above to find the optical power along the antenna

$$\frac{\mathcal{P}(z)}{\mathcal{P}_0} = e^{-a\left(e^{\zeta}-1\right)} \tag{50}$$

where we've introduced two dimensionless parameters: the local scattering rate at the beginning of the antenna $a = -\alpha_{\mathrm{m}} \mathcal{P}_{\mathrm{m}0} e^{-\gamma L}/\gamma$ and the distance along the antenna $\zeta = \gamma z$. The power radiated from the waveguide is computed from the guided power by taking the derivative $\mathcal{P}_{\mathrm{r}} = -\partial_z \mathcal{P}$ yielding

$$\frac{\mathcal{P}_{\mathrm{r}}(\zeta)}{\gamma \mathcal{P}_0} = a \exp\left(\zeta - a\left(e^{\zeta} - 1\right)\right). \tag{51}$$

Maximal scattering occurs at $\zeta_{\max} = -\log a$. When the optical scattering rate at $z = 0$ is large compared to the mechanical attenuation rate γ such that $\zeta_{\max} \ll 0$, the power radiated $\mathcal{P}_{\mathrm{r}}$ decays exponentially and attenuation can be ignored. As a is decreased perhaps by lowering $\mathcal{P}_{\mathrm{m}0}$, the maximum shifts right $\zeta_{\max}$ and when sufficiently far from the origin and for sufficiently long antennas the resulting radiation pattern has a FWHM of $\Delta\zeta = 2.45$. The $1/e$ width is 3 and the $1/e^2$ width is 4.45. Figure 9 shows the mechanical power necessary to achieve a particular radiation pattern for an antenna of a particular length.

Appendix F Derivation of antenna properties

Here we provide derivations of the antenna properties presented in the main text. Some of the properties are illustrated in Fig. 10.

F.1 Field of view

The field of view $\Delta\theta$ is the range of angles than can be reached by sweeping the mechanical frequency. It is set by the bandwidth of the electromechanical transducer, the sensitivity of the mechanical wavevector to frequency as well as the sensitivity of radiation wavevector to mechanical wavevector. In particular, subtracting the phase-matching conditions at two different mechanical frequencies leads to

$$k(\omega_{\mathrm{r}} + \Delta\Omega)\cos(\theta + \Delta\theta) - k(\omega_{\mathrm{r}})\cos(\theta) = -\Delta K \tag{52}$$

with $\Delta\Omega = v_{\mathrm{m}} \Delta K$ the bandwidth of the electromechanical transducer. This determines $\Delta\theta$ in general, while for small $\Delta\theta$ we get

$$\Delta\theta = \frac{\Delta\Omega}{k\sin(\theta)}\left(\frac{1}{v_{\mathrm{m}}} + \frac{\cos(\theta)}{c}\right) \tag{53}$$

$$\approx \frac{\Delta\Omega}{k\sin(\theta) v_{\mathrm{m}}} = \frac{\Delta\Omega}{2\pi}\frac{\lambda}{\sin(\theta) v_{\mathrm{m}}} \tag{54}$$

with $\lambda = 2\pi/k$ the radiation's wavelength. Here we used $c \gg v_{\mathrm{m}}$.

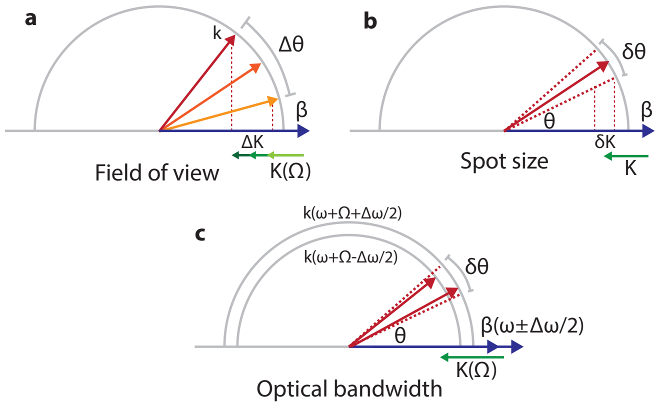

Fig. 10. (a), The field of view $\Delta\theta$ is the range of angles that can be reached by tuning the mechanical frequency Ω at fixed optical frequency ω. (b) The spot size $\delta\theta$ is the angular width – set by the wavevector uncertainty δK – of the scattered optical beam in the far field. (c) The optical bandwidth at each spot $\Delta\omega$ is the amount the optical frequency ω can be shifted before the beam angle shifts by more than the spot size $\delta\theta$ at fixed mechanical frequency Ω. Since both the outgoing wavevector k and the guided wavevector β change with frequency, the optical bandwidth at each spot $\Delta\omega$ is set by the walk-off between the guided and radiating optical fields.

F.2 Spot size

The spot size $\delta\theta$ is the angular width of the scattered optical beam in the far field. It is set by the wavevector uncertainty $\delta K = \frac{2\pi}{L_{\text{eff}}}$ corresponding to the finite aperture:

$$\begin{aligned} k\,\delta\cos(\theta) &\approx k\sin(\theta)\delta\theta \\ &= \delta K = \frac{2\pi}{L_{\text{eff}}} \end{aligned} \tag{55}$$

where we dropped a minus sign. Therefore,

$$\delta\theta = \frac{\lambda}{\sin(\theta)L_{\text{eff}}} \tag{56}$$

F.3 Number of resolvable spots

The number of resolvable spots N_θ is the ratio between the field of view $\Delta\theta$ and the spot size $\delta\theta$. Neglecting the frequency-dependence of k allows us to express $N_\theta = \Delta K/\delta k$ only in terms of the mechanical properties of the optomechanical antenna. We find that

$$N_\theta = \frac{\Delta K}{\delta k} = \frac{\Delta\theta}{\delta\theta} = \frac{\Delta\Omega}{2\pi}\tau_{\text{m}}. \tag{57}$$

The number of resolvable spots is set by the product of the transducer bandwidth $\Delta\Omega$ and the mechanical transit time $\tau_{\text{m}} = L_{\text{eff}}/v_{\text{m}}$. With a large bandwidth transducer we have $\Delta K \longrightarrow 2k$ and therefore $N_\theta \longrightarrow 2\frac{L_{\text{eff}}}{\lambda}$ – making the effective aperture length the ultimate limit on the number of resolvable spots.

F.4 Bandwidth at each spot

The optical bandwidth is set by how much the optical frequency can be changed before the beam angle disperses more than the spot size. For fixed K we differentiate the phase-matching condition and

$$\cos\theta\,\delta k + \underbrace{k\,\delta\cos\theta}_{=\delta K} = \delta\beta. \tag{58}$$

We equate the second term, the angular variation from changing ω, to the angular spread of the beam in section F.2 $\delta K = \frac{2\pi}{L_{\mathrm{eff}}}$. Relating $\delta\beta$ and δk to $\Delta\omega$ by the guided and free-space optical dispersion relations we find

$$\frac{\Delta\omega}{2\pi} = \frac{1}{\tau - \tau_{\mathrm{r}}} \tag{59}$$

with $\tau = L_{\mathrm{eff}} n_{\mathrm{g}}/c$ the transit time of the guided optical wave and $\tau_{\mathrm{r}} = L_{\mathrm{eff}}\cos\theta/c$ the transit time of the radiation mode across the aperture and n_{g} the group index of the guided optical wave. The optical bandwidth at each spot $\Delta\omega_0$ is thus set by the walk-off between the guided and the radiation mode.

A similar derivation as in the optical case above shows that the mechanical transit time determines the mechanical bandwidth at each spot

$$\frac{\Delta\Omega_{\mathrm{m}}}{2\pi} = \frac{1}{\tau_{\mathrm{m}}} \tag{60}$$

Funding

National Science Foundation (NSF) (ECCS-1509107, ECCS-1808100); Stanford University (Terman Fellowship, Hellman fellowship, start-up funds from the school of Humanities and Sciences); ONR (QOMAND MURI); VOCATIO; Horizon 2020 with Research Foundation – Flanders (FWO) (Marie Skłodowska-Curie 665501).

Acknowledgments

We thank Patricio Arrangoiz-Arriola, Okan Atalar, Rishi Patel, and Jeremy Witmer for helpful discussions.

References

1. K. Van Acoleyen, K. Komorowska, W. Bogaerts, and R. Baets, "One-dimensional off-chip beam steering and shaping using optical phased arrays on silicon-on-insulator," Journal of Lightwave Technology **29**, 3500–3505 (2011).
2. J. K. Doylend, M. J. R. Heck, J. T. Bovington, J. D. Peters, M. L. Davenport, L. a. Coldren, and J. E. Bowers, "Hybrid III/V silicon photonic source with integrated 1D free-space beam steering," Optics Letters **37**, 4257 (2012).
3. J. K. Doylend, M. J. R. Heck, J. T. Bovington, J. D. Peters, L. A. Coldren, and J. E. Bowers, "Two-dimensional free-space beam steering with an optical phased array on silicon-on-insulator," Optics Express **19**, 21595 (2011).
4. K. Van Acoleyen, W. Bogaerts, and R. Baets, "Two-dimensional dispersive off-chip beam scanner fabricated on silicon-on-insulator," IEEE Photonics Technology Letters **23**, 1270–1272 (2011).
5. J. C. Hulme, J. K. Doylend, M. J. R. Heck, J. D. Peters, M. L. Davenport, J. T. Bovington, L. A. Coldren, and J. E. Bowers, "Fully integrated hybrid silicon two dimensional beam scanner," Optics Express **23**, 5861 (2015).
6. C. V. Poulton, A. Yaccobi, Z. Su, M. J. Byrd, and M. R. Watts, "Optical phased array with small spot size, high steering range and grouped cascaded phase shifters," in "Integrated Photonics Research, Silicon and Nanophotonics," (Optical Society of America, 2016), pp. IW1B–2.
7. J. Sun, E. Timurdogan, A. Yaacobi, E. S. Hosseini, and M. R. Watts, "Large-scale nanophotonic phased array," Nature **493**, 195–199 (2013).
8. M. J. Heck, "Highly integrated optical phased arrays: photonic integrated circuits for optical beam shaping and beam steering," Nanophotonics **6**, 93–107 (2016).
9. D. Kedar and S. Arnon, "Urban optical wireless communication networks: the main challenges and possible solutions," IEEE Communications Magazine **42**, S2–S7 (2004).
10. H. Elgala, R. Mesleh, and H. Haas, "Indoor optical wireless communication: potential and state-of-the-art," IEEE Communications Magazine **49**, 56–62 (2011).
11. W. S. Rabinovich, C. I. Moore, R. Mahon, P. G. Goetz, H. R. Burris, M. S. Ferraro, J. L. Murphy, L. M. Thomas, G. C. Gilbreath, M. Vilcheck, and M. R. Suite, "Free-space optical communications research and demonstrations at the US Naval Research Laboratory," Applied Optics **54**, F189 (2015).
12. C. Quate, C. Wilkinson, and D. Winslow, "Interaction of light and microwave sound," Proceedings of the IEEE **53**, 1604–1623 (1965).

13. E. Gordon, “A review of acoustooptical deflection and modulation devices,” Proceedings of the IEEE **54**, 1391–1401 (1966).
14. A. Korpel, R. Adler, P. Desmares, and W. Watson, “A Television Display Using Acoustic Deflection and Modulation of Coherent Light,” Proceedings of the IEEE **54**, 1429–1437 (1966).
15. F. R. Gfeller, “A colinear thin-film acousto-optic scanner,” Journal of Physics D: Applied Physics **10** (1977).
16. A. Matteo, C. Tsai, and N. Do, “Collinear guided wave to leaky wave acoustooptic interactions in proton-exchanged LiNbO/sub 3/ waveguides,” IEEE Transactions on Ultrasonics, Ferroelectrics and Frequency Control **47**, 16–28 (2000).
17. D. E. Smalley, Q. Y. J. Smithwick, V. M. Bove, J. Barabas, and S. Jolly, “Anisotropic leaky-mode modulator for holographic video displays.” Nature **498**, 313–7 (2013).
18. E. A. Kittlaus, H. Shin, and P. T. Rakich, “Large Brillouin amplification in silicon,” Nature Photonics **10**, 463–467 (2016).
19. R. Van Laer, B. Kuyken, D. Van Thourhout, and R. Baets, “Interaction between light and highly confined hypersound in a silicon photonic nanowire,” Nature Photonics **9**, 199–203 (2015).
20. C. J. Sarabalis, J. T. Hill, and A. H. Safavi-Naeini, “Guided acoustic and optical waves in silicon-on-insulator for Brillouin scattering and optomechanics,” APL Photonics **1**, 071301 (2016).
21. M. Aspelmeyer, T. J. Kippenberg, and F. Marquardt, “Cavity optomechanics,” Reviews of Modern Physics **86**, 1391–1452 (2014).
22. B. Eggleton, C. Poulton, and R. Pant, “Inducing and harnessing stimulated Brillouin scattering in photonic integrated circuits,” Advances in Optics and Photonics pp. 536–587 (2013).
23. R. Van Laer, A. Bazin, B. Kuyken, R. Baets, and D. Van Thourhout, “Net on-chip Brillouin gain based on suspended silicon nanowires,” New Journal of Physics **17**, 115005 (2015).
24. B. E. A. Saleh and M. C. Teich, *Fundamentals of Photonics*, Wiley Series in Pure and Applied Optics (John Wiley & Sons, Inc., 1991).
25. D. Marcuse, “Mode Conversion Caused by Surface Imperfections of a Dielectric Slab Waveguide,” Bell System Technical Journal **48**, 3187–3215 (1969).
26. D. Marcuse, “Radiation Losses of Dielectric Waveguides in Terms of the Power Spectrum of the Wall Distortion Function,” Bell System Technical Journal **48**, 3233–3242 (1969).
27. C. J. Sarabalis, Y. D. Dahmani, R. N. Patel, J. T. Hill, and A. H. Safavi-Naeini, “Release-free silicon-on-insulator cavity optomechanics,” Optica **4**, 1147 (2017).
28. R. Van Laer, R. N. Patel, T. P. McKenna, J. D. Witmer, and A. H. Safavi-Naeini, “Electrical driving of X-band mechanical waves in a silicon photonic circuit,” arXiv:1806.04100 pp. 1–33 (2018).
29. J. M. Elson and J. M. Bennett, “Calculation of the power spectral density from surface profile data,” Applied Optics **34** (1995).
30. S. Selvaraja, W. Bogaerts, P. Dumon, D. Van Thourhout, and R. Baets, “Subnanometer Linewidth Uniformity in Silicon Nanophotonic Waveguide Devices Using CMOS Fabrication Technology,” IEEE Journal of Selected Topics in Quantum Electronics **16**, 316–324 (2010).
31. O. Fursenko, J. Bauer, A. Knopf, S. Marschmeyer, L. Zimmermann, and G. Winzer, “Characterization of Si nanowaveguide line edge roughness and its effect on light transmission,” Materials Science and Engineering B: Solid-State Materials for Advanced Technology **177**, 750–755 (2012).
32. D. Melati, A. Melloni, and F. Morichetti, “Real photonic waveguides: guiding light through imperfections,” Advances in Optics and Photonics **6**, 156–224 (2014).
33. D. Engström, J. Bengtsson, E. Eriksson, and M. Goksör, “Improved beam steering accuracy of a single beam with a 1D phase-only spatial light modulator.” Optics express **16**, 18275–18287 (2008).
34. B.-W. Yoo, M. Megens, T. Chan, T. Sun, W. Yang, C. J. Chang-Hasnain, D. a. Horsley, and M. C. Wu, “Optical phased array using high contrast gratings for two dimensional beamforming and beamsteering,” Opt. Express **21**, 12238–12248 (2013).
35. M. Megens, B.-W. Yoo, T. Chan, W. Yang, T. Sun, C. J. Chang-Hasnain, M. C. Wu, and D. A. Horsley, “High-speed 32×32 MEMS optical phased array,” International Society for Optics and Photonics **8977**, 89770H (2014).
36. A. Tuantranont, V. M. Bright, J. Zhang, W. Zhang, J. A. Neff, and Y. C. Lee, “Optical beam steering using MEMS-controllable microlens array,” Sensors and Actuators A: Physical **91**, 363–372 (2001).
37. T. Zhang, J. L. Abellan, A. Joshi, and A. K. Coskun, “Thermal management of manycore systems with silicon-photonic networks,” in “Design, Automation & Test in Europe Conference & Exhibition (DATE), 2014,” (IEEE Conference Publications, New Jersey, 2014), pp. 1–6.
38. Y. Shi, S. Han, and S. Fan, “Optical Circulation and Isolation Based on Indirect Photonic Transitions of Guided Resonance Modes,” ACS Photonics **4**, 1639–1645 (2017).
39. W. S. Rabinovich, P. G. Goetz, M. Pruessner, R. Mahon, M. S. Ferraro, D. Park, E. Fleet, and M. J. DePrenger, “Free space optical communication link using a silicon photonic optical phased array,” Proc. SPIE **9354**, 93540B (2015).
40. D. E. Smalley, “Holovideo on a Stick: Integrated Optics for Holographic Video Displays,” Ph.D. thesis, Massachusetts Institute of Technology (2013).
41. C. K. Wang and W. D. Philpot, “Using airborne bathymetric lidar to detect bottom type variation in shallow waters,” Remote Sensing of Environment **106**, 123–135 (2007).
42. A. Schliesser, N. Picqué, and T. Hänsch, “Mid-infrared frequency combs,” Nature Photonics **6** (2012).

43. S. Boudreau, S. Levasseur, C. Perilla, S. Roy, and J. Genest, “Chemical detection with hyperspectral lidar using dual frequency combs.” Optics express **21**, 7411–8 (2013).
44. F. Aflatouni, B. Abiri, A. Rekhi, and A. Hajimiri, “Nanophotonic coherent imager,” Optics Express **23**, 5117 (2015).
45. R. Fatemi, B. Abiri, and A. Hajimiri, “An 8 × 8 heterodyne lens-less opa camera,” in “CLEO: QELS_Fundamental Science,” (Optical Society of America, 2017), pp. JW2A–9.
46. COMSOL Multiphysics v5.0. www.comsol.com. COMSOL AB, Stockholm, Sweden.
47. D. Taillaert, “Grating couplers as Interface between Optical Fibres and Nanophotonic Waveguides,” Ph.D. thesis, Ghent University (2005).
48. F. V. Laere, S. Member, T. Claes, J. Schrauwen, S. Scheerlinck, W. Bogaerts, and D. Taillaert, “Compact Focusing Grating Couplers for Silicon-on-Insulator Integrated Circuits,” IEEE Photonics Technology Letters **19**, 1919–1921 (2007).
49. B. E. Little, “A variational coupled-mode theory including radiation loss for grating-assisted couplers,” Journal of Lightwave Technology **14**, 188–195 (1996).
50. Lumerical Inc. http://www.lumerical.com/tcad-products/fdtd/.
51. P. Rakich, C. Reinke, R. Camacho, P. Davids, and Z. Wang, “Giant Enhancement of Stimulated Brillouin Scattering in the Subwavelength Limit,” Physical Review X **2**, 1–15 (2012).
52. S. G. Johnson, M. Ibanescu, M. A. Skorobogatiy, O. Weisberg, J. D. Joannopoulos, and Y. Fink, “Perturbation theory for Maxwell’s equations with shifting material boundaries,” Physical Review E **65**, 066611 (2002).
53. R. Van Laer, R. Baets, and D. Van Thourhout, “Unifying Brillouin scattering and cavity optomechanics,” Physical Review A **93**, 15 (2016).
54. R. W. Dixon, “Photoelastic Properties of Selected Materials and Their Relevance for Applications to Acoustic Light Modulators and Scanners,” Journal of Applied Physics **38**, 5149–5153 (1967).
55. S. G. Johnson, M. L. Povinelli, M. Soljačić, A. Karalis, S. Jacobs, and J. D. Joannopoulos, “Roughness losses and volume-current methods in photonic-crystal waveguides,” Applied Physics B **81**, 283–293 (2005).
56. S. K. Selvaraja, “Wafer-Scale Fabrication Technology for Silicon Photonic Integrated Circuits,” Ph.D. thesis, Ghent University (2011).
57. K. K. Lee, D. R. Lim, H.-C. Luan, A. Agarwal, J. Foresi, and L. C. Kimerling, “Effect of size and roughness on light transmission in a Si/SiO_2 waveguide: Experiments and model,” Applied Physics Letters **77**, 1617 (2000).
58. Y. Yang, Y. Ma, H. Guan, Y. Liu, S. Danziger, S. Ocheltree, K. Bergman, T. Baehr-Jones, and M. Hochberg, “Phase coherence length in silicon photonic platform,” Optics Express **23**, 16890 (2015).
59. C. Wolff, R. Van Laer, M. Steel, B. Eggleton, and C. Poulton, “Brillouin resonance broadening due to structural variations in nanoscale waveguides,” New Journal of Physics **18**, 1–9 (2016).
60. A. A. Clerk, M. H. Devoret, S. M. Girvin, F. Marquardt, and R. J. Schoelkopf, “Introduction to quantum noise, measurement, and amplification,” Reviews of Modern Physics **82**, 1155–1208 (2010).
61. S. Ghaffari, S. A. Chandorkar, S. Wang, E. J. Ng, C. H. Ahn, V. Hong, Y. Yang, and T. W. Kenny, “Quantum Limit of Quality Factor in Silicon Micro and Nano Mechanical Resonators,” Scientific Reports **3**, 3244 (2013).